Research on Correction Method for Pipe-Soil p-y Curves in Submarine Silty Clay-Sand Gas Hydrate Formations

Haoyu Diao[1], Yan Xia[1,*], Bangchen Wu[2], Fansheng Ban[1], Li Fu[1], Henglin Yang[1], Kailong Wang[1], Aiguo He[1], Xiangyang Wang[1], Pan Fu[1], Hao Wang[3], Chaowei Li[4] and Song Deng[4]

[1] CNPC Engineering Technology R&D Company Limited, Beijing, 102206, China

[2] Institute of Geomechanics, Chinese Academy of Geological Sciences, Beijing, 100081, China

[3] PetroChina Liaohe Oilfield Company, Panjin, 124010, China

[4] School of Petroleum and Natural Gas Engineering, Changzhou University, Changzhou, 213164, China

INFORMATION

Keywords:
Hydrated argillaceous silt
triaxial compression experiment
mechanical properties
numerical simulation
p-y curve

DOI: 10.23967/j.rimni.2025.10.70728

SCIPEDIA Revista Internacional de Métodos Numéricos para Cálculo y Diseño en Ingeniería

Revista Internacional Métodos numéricos para cálculo y diseño en ingeniería RIMNI

In cooperation with CIMNE

Research on Correction Method for Pipe-Soil p-y Curves in Submarine Silty Clay-Sand Gas Hydrate Formations

Haoyu Diao[1], Yan Xia[1,*], Bangchen Wu[2], Fansheng Ban[1], Li Fu[1], Henglin Yang[1], Kailong Wang[1], Aiguo He[1], Xiangyang Wang[1], Pan Fu[1], Hao Wang[3], Chaowei Li[4] and Song Deng[4]

[1]CNPC Engineering Technology R&D Company Limited, Beijing, 102206, China

[2]Institute of Geomechanics, Chinese Academy of Geological Sciences, Beijing, 100081, China

[3]PetroChina Liaohe Oilfield Company, Panjin, 124010, China

[4]School of Petroleum and Natural Gas Engineering, Changzhou University, Changzhou, 213164, China

ABSTRACT

The development of marine natural gas hydrates faces complex geomechanical challenges. Argillaceous silty hydrate reservoirs, due to their weak cementation and low permeability, have significantly different mechanical properties from those of general reservoirs. Based on the self-developed triaxial seepage experimental platform for hydrates, this paper systematically carried out triaxial compression experiments of argillaceous silt hydrate sediments, focusing on simulating the *in-situ* temperature and pressure conditions of the formation, analyzing the influences of saturation, temperature and confining pressure on mechanical properties, and comparing them with the experimental results of sandy hydrate sediments. The experimental results show that due to the weak cementation effect of kaolin and methane hydrate, the failure mode of argillaceous silt hydrate is manifested as compression and dispersion, while sandy hydrate presents the traditional core compression failure characteristics. The peak strength of the stress-strain curve of argillaceous silt hydrate is lower than that of sandy hydrate, and the strain softening characteristic is more significant. The experimental results were calculated through MATLAB programming, and it was obtained that the cohesion and internal friction Angle of the argillaceous silt hydrate increased with saturation higher than those of the sandy hydrate. The pipe-soil coupling numerical simulation based on ABAQUS reveals that the initial stiffness and plastic deformation response of the p-y curve in the argillaceous silty hydrate formation are essentially different from those in the traditional API sandy soil model. By comparing the numerical simulation results of sandy properties and argillaceous silty hydrate, a two-parameter correction model for argillaceous silty strata was proposed. The cementation factor related to mass abundance and the displacement correction term were introduced. The error analysis indicated that the correction method was significantly superior to the API specification. Studies show that the mechanical properties of hydrates need to be evaluated independently, and the correction method provides a theoretical basis for the safety design of deep water well engineering.

OPEN ACCESS

Received: 22/07/2025

Accepted: 23/10/2025

DOI
10.23967/j.rimni.2025.10.70728

Keywords:
Hydrated argillaceous silt
triaxial compression experiment
mechanical properties
numerical simulation
p-y curve

*Correspondence: Yan Xia (xiayan0722@163.com).

1 Introduction

Natural gas hydrate is a cage-like compound formed under low-temperature and high-pressure conditions [1−2]. Compared with traditional fossil energy, it has advantages such as large reserves, wide distribution, and low combustion pollution. It is widely enriched in the onshore permafrost zone and the shallow seabed strata at the edge of the continental shelf [3−6]. Its large-scale development could optimize the national energy structure, currently dominated by non-clean energy sources such as coal and oil. This would provide strong support for long-term energy supply security and environmental protection. [7]. Natural gas hydrates in China's sea areas mainly occur in unconsolidated diagenetic sediments such as silty sand, clayey silty sand and silty clay [8]. The two offshore natural gas hydrate test production operations in 2017 and 2019 were both targeted at argillaceous silt-sand type natural gas hydrate reservoirs. This type of reservoir is the main production area of hydrates in China, characterized by large reserves, shallow burial (<400 m), and low reservoir permeability ($<10 \times 10^{-3}$ μm^2). It is also recognized as the hydrate reservoir type with the greatest extraction difficulty [9]. Therefore, conducting in-depth systematic research on the mechanical properties of argillaceous silt hydrate sediments is of great practical significance for scientifically assessing the development potential of natural gas hydrate resources and ensuring the safe operation of seabed engineering.

Some studies have been conducted on the mechanical properties of hydrate sediments and shallow seabed strata. Liu et al. [10] studied the characteristics of the natural gas hydrate sediment samples obtained in the Pearl River Mouth Basin in 2013. They found that the sediment particles were mainly silt and clay, the hydrate structure was type I hydrate structure, the guest molecules were mainly methane (>99.9%), and the occupancy rates of large and small cages were 99.5% and 91.4%, respectively. The hydration number is 5.9. Yoneda et al. [11] studied the soil and mechanical properties of hydrate sediment samples obtained from Eastern Nankai Trough, Japan's first offshore production experimental area, and found that porosity decreased with increasing depth. It was also found that the strength and stiffness of sandy hydrate sediments increased with the increase of hydrate saturation. Furthermore, consolidated drained and undrained triaxial compression experiments on hydrate sediments from NGHP-02 revealed that their strength is highly dependent on the strain rate [12]. Delli et al. [13] proposed a weighted combination hybrid method based on the existing permeability models and evaluated the predictive performance of various permeability models using the results of indoor experiments and field permeability tests. Roosta et al. [14] investigated the effects of surfactants such as sodium dodecyl sulfate (SDS) and thermodynamic additives such as tetrahydrofuran (THF) on the kinetics of methane hydrate formation, and determined the kinetic parameters of methane hydrate formation in the chemical affinity model with and without additives. Chen et al. [15], based on the hydrate parameters at the SH7-B station in the Shenhu area of the South China Sea, artificially synthesized hydrates and conducted triaxial shear experiments. They established the expression for the linear increase of shear strength with the effective confining pressure and hydrate saturation. Meanwhile, they introduced saturation as a parameter into the Mohr-Coulomb criterion. The strength criteria applicable to the mining process have been established. Zhao et al. [16] used clay and quartz sand samples extracted from the South China Sea to synthesize clay silage hydrate sediment samples indoors and studied the effects of effective stress, seepage pressure difference and saturation on permeability. They found that permeability decreased with the increase of effective stress and saturation. Lu and Zhang [17] proposed that the lateral behavior of the tube-soil system might be affected by axial loads, established the p-y curve model of longitudinally and laterally loaded piles in sandy soil, and proposed the determination method of parameters. The validity of the p-y model and the parameter determination method was verified by comparing with the numerical simulation results. Zhu et al. [18] analyzed the tube-soil interaction based on the stress-strain relationship of small

strain using the total displacement load Extended movable strength Design (T-EMSD), proposed an analytical p-y curve model, and verified it by finite element numerical simulation. Chang and Hutchinson [19] conducted an experimental study on the p-y curves of liquefiable soil. Through reverse calculation and normalization, they presented the p-y curves under different super-pore pressures and proposed an empirical equation for fitting the p-y curves of partially liquefiable soil. Dash et al. [20] studied the liquefaction of saturated sandy soil under seismic action and proposed a new p-y curve correction method. Lim and Jeong [21] studied the interaction between the pile foundation system and dry sand by experimental methods and proposed a simplified hyperbolic p-y curve.

Due to the unique mechanical properties of hydrate sediments, the p-y curves for shallow seabed hydrate-bearing strata differ significantly from those of traditional shallow seabed strata. Based on the API standards, the calculation method for the p-y curve of shallow seabed hydrate-bearing strata is revised. This revision holds significant theoretical and practical importance for enhancing the safety of offshore drilling and completion operations. In this paper, through the self-developed hydrate triaxial-permeability experimental platform, uniaxial compression and triaxial shear tests were conducted on sandy and silty clay-sand hydrate sediments with different saturations and mass abundances under various temperature and pressure conditions. Based on the obtained stress-strain curves, mechanical parameters such as Poisson's ratio and Young's modulus were calculated, and the effects of saturation (mass abundance), temperature, and pressure on the strength of hydrate sediments were analyzed. Cohesion and internal friction angle of silty clay-sand hydrate sediments were calculated using MATLAB programming. Numerical simulations under actual working conditions were performed using ABAQUS, yielding p-y curves for hydrate-bearing strata with different saturations. A modification method for the p-y curve of hydrate-bearing strata was proposed based on the p-y curve in the API specification. The accuracy of the modification method was validated through error analysis.

2 Experimental Study on the Mechanical Properties of Sediments in Hydrate-Bearing Strata

Marine natural gas hydrate reservoirs can be classified into two types according to lithology: consolidated diagenesis and weakly cemented non-diagenesis. The consolidated diagenetic hydrate layer is supported by the formation framework. After the hydrate decomposes, the reservoir does not deform or deforms slightly. Due to the poor cementation of the formation framework, non-diagenetic hydrates cannot provide complete support. Therefore, hydrates have to undertake part of the reservoir support. After the decomposition of hydrates, the reservoir will collapse or deform. Previous experiments have been conducted on sandy hydrate sediments [22]. To conduct a comprehensive study of hydrate sediments, this paper mainly uses non-diagenetic (argillaceous silt) hydrate sediments with poor cementation strength for experimental tests.

2.1 Hydrate-Bearing Sediments Preparation Device

The main body of the hydrate sediment preparation device adopted in this paper is the hydrate sediment preparation kettle (Fig. 1).

The pressure control system of the preparation device consists of two parts: the axial pressure control system and the pneumatic pressure control system. The axial pressure control system controls the pressure through a hydraulic pump and can provide the necessary pressure conditions for the compaction of hydrate deposits. The pneumatic control system consists of a vacuum pump and a gas cylinder. Before the reaction, the vacuum pump is used to evacuate the preparation device to avoid interference from other gases. Then, the experimental gas is introduced through the gas cylinder to control the gas pressure inside the device, which can provide the necessary pressure conditions for the formation of hydrates.

Figure 1: Hydrate sediment preparation kettle

The temperature control system of the preparation device circulates the antifreeze through an external temperature control device to achieve temperature control of the preparation kettle, which can provide the necessary temperature conditions for the formation of hydrates. A liquid circulation channel is preset inside the wall of the preparation reactor for the circulation of the refrigerant.

2.2 Triaxial Seepage Experimental Platform for Hydrates

Fig. 2 shows the triaxial seepage experimental platform for hydrates. All components, except for the support and gas cylinders, are linked to a computer for control purposes. The axial pressure loading system is hydraulically operated for applying pressure. The support mechanism is of the column type. The temperature control system uses antifreeze as its circulating liquid medium. Both the injection and output systems utilize gas as their fluid medium [22].

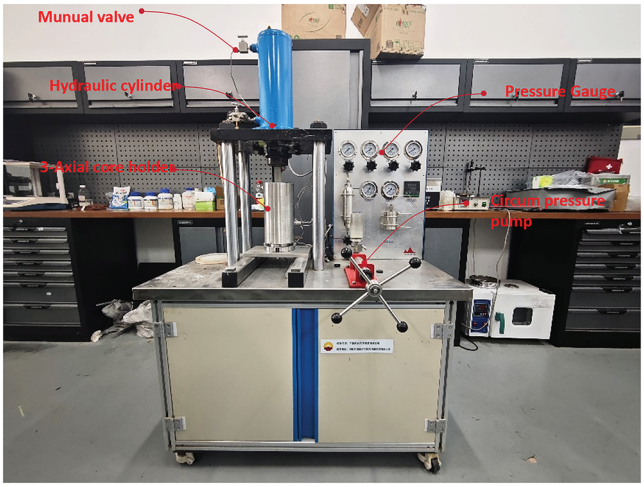

Figure 2: Platform of the triaxial seepage experimental device for hydrates

2.3 Preparation Materials and Methods for Hydrate Sediments

In this paper, the *in-situ* generation method is adopted to prepare hydrate sediments. The commonly used hydrate preparation methods include the *in-situ* generation method and the mixed sample preparation method. Compared with the mixed sample preparation method, the *in-situ* generation method is closer to the real conditions of hydrate formation, and the measured data are closer to the real hydrate sediments. Meanwhile, in order to accurately control the formation amount of hydrates, the gas saturation method is adopted for the preparation of hydrate sediments during the process of hydrate sediment preparation.

Due to the extremely low solubility of methane gas in water, in the preparation process, a 0.3 g/L SDS (sodium dodecyl sulfate) solution was used instead of pure deionized water to increase the solubility of methane in water and promote the formation of methane hydrates [14].

(1) Prepare materials

The materials used for preparing hydrate sediments include methane gas, quartz sand, kaolin and sodium dodecyl sulfate solution (SDS).

The sediment particles for the argillaceous silt hydrate samples consist of kaolin with a particle diameter of 5 μm and quartz sand with a particle diameter of 50 μm, mixed in a 2:1 ratio by mass. Since the formation of hydrates can clog the pore structure of some sediment systems, there will be some residual water that cannot react with methane to form hydrates. Therefore, a 3% increment of SDS solution is added during the preparation to ensure that the saturation of the prepared hydrate sediment reaches the preset value.

(2) Preparation methods of sandy hydrate sediments

The preparation of sandy natural gas hydrate sediments in this study refers to the method described in reference [22].

(3) Preparation method of hydrated sediment of silty silt

The hydrated sediment of argillaceous silt was prepared using quartz sand and kaolin, without the need to add epoxy resin for cementation. Because the formation framework of weakly cemented undiagenetic natural gas hydrate reservoirs is poorly cemented, natural gas hydrates play the role of the main framework of the reservoir.

The specific method for preparing hydrated sediment of silky sand: Firstly, use a standard screen to screen quartz sand with a particle size of 50 μm and kaolin with a particle size of 5 μm for standby, and lay a filter screen at the bottom of the preparation pot to prevent sand from entering the gas channel. Meanwhile, weigh a certain amount of deionized water for later use. Next, 23.66 g of quartz sand and 11.34 g of kaolin were weighed using an electronic analytical balance. After thorough mixing, they were placed in the preparation kettle and sealed by connecting the axial pressure control system. Start the temperature control system and adjust the temperature of the preparation device to the set temperatures (2°C, 4°C, 8°C and 12°C, respectively). Subsequently, the axial pressure control system was activated to pressurize the preparation device, setting the pressure at 15 MPa until the deformation no longer changed. Connect the preparation kettle to the vacuum pump and evacuate the kettle to a vacuum state. Then, connect the preparation kettle to the cross-flow pump, inject a certain amount of deionized water into the preparation kettle, and use a vacuum to draw the deionized water into the preparation kettle and distribute it evenly. Next, connect the preparation device to the gas cylinder, introduce methane gas, and maintain the pressure inside the preparation kettle at the set pressure (5, 10 and 12 MPa, respectively). Finally, when the gas cylinder valve is closed, if the pressure inside

the preparation kettle can be maintained stable for a long time, the preparation process is completed. The prepared hydrated sediment of argillaceous silt is shown in Fig. 3.

Figure 3: Clayey-silt hydrate sediment sample

2.4 Experimental Steps

The triaxial compression experiment was carried out in accordance with the following process, specifically including:

(1) Activate the temperature control system of the hydrate triaxial-seepage experimental platform to reduce the temperature inside the reactor to the experimentally set temperature;

(2) Fill the hydrate deposits into rubber sleeves with the same inner diameter and a thickness of 0.5 mm, and connect the top to the top plug to avoid the influence of pressurized liquid on the properties;

(3) Insert the back pressure plug into the rubber sleeve, rotate the sealed reactor, and start the axial pressure loading system to fix the hydrate deposits;

(4) Start the confining pressure loading system to load the confining pressure to the set value (at least 0.2 MPa greater than the pore pressure);

(5) Start the injection system to apply the loading back pressure (pore pressure) to the set value;

(6) Use the axial pressure loading system to apply axial pressure to the hydrate sediment until it breaks;

(7) When the gas cylinder valve is closed, if the pressure inside the preparation vessel can remain stable for a long time, the preparation process is considered complete.

(8) Unload the back pressure, confining pressure and axial pressure in sequence and remove the sediment.

To reduce the decomposition of hydrates during the preparation of the hydrate-bearing sediment model, the experiment was conducted in a freezer at –20°C.

2.5 Experimental Phenomenon of Triaxial Compression

Triaxial compression experiments were conducted on sandy hydrate sediments, and a relatively good compression failure phenomenon was presented (Fig. 4), which is similar to the traditional triaxial compression failure phenomenon of the core.

Figure 4: Triaxial shear test phenomenon of sand hydrate sediment samples [22]

Triaxial compression experiments were conducted on the hydrated sediment of argillaceous silt, and the failure phenomenon was that it was basically crushed apart (Fig. 5). The reason for the different triaxial compression test failure phenomena of sandy and argillaceous silt hydrate sediments is that the cementing effect of hydrates and kaolin on argillaceous silt hydrate sediments is much smaller than that of epoxy resin on sandy hydrate sediments.

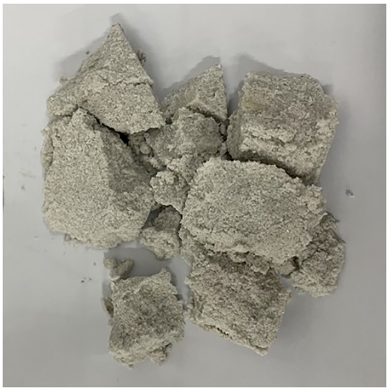

Figure 5: Triaxial shear test phenomenon of clayey-silt hydrate sediment samples

2.6 Experimental Results and Analysis of Hydrate Sediments

Due to the displacement of the original sediment particles during the synthesis of clayey silt hydrates, which disrupts the original sediment pore structure, the use of average mass abundance to characterize the hydrate content is more accurate. The definition of average mass abundance is the percentage of hydrates in the sediment-hydrate mixed system mass, which can be calculated by Eq. (1).

$$\begin{cases} R_{\mathrm{mh}} = \dfrac{m_{\mathrm{h}}}{m_{\mathrm{h}} + m_{\mathrm{sand}} + \mathrm{m}_{\mathrm{soil}} + m_{\mathrm{wf}}} \times 100\% = \dfrac{\dfrac{M_{\mathrm{h}} m_{\mathrm{m}}}{M_{\mathrm{m}}}}{\dfrac{M_{\mathrm{h}} m_{\mathrm{m}}}{M_{\mathrm{m}}} + m_{\mathrm{sand}} + \mathrm{m}_{\mathrm{soil}} + m_{\mathrm{wf}}} \times 100\% \\ m_{\mathrm{wf}} = m_{\mathrm{l}} - \dfrac{N_{\mathrm{h}} M_{\mathrm{l}} m_{\mathrm{m}}}{M_{\mathrm{m}}} \\ R_{\mathrm{mw}} = 1 - R_{\mathrm{mh}} - R_{\mathrm{ms}} = \dfrac{m_{\mathrm{wf}}}{m_{\mathrm{h}} + m_{\mathrm{sand}} + \mathrm{m}_{\mathrm{soil}} + m_{\mathrm{wf}}} \times 100\% \end{cases} \tag{1}$$

In the equation, R_{mh} represents the average mass abundance of clayey silt hydrate sediment; m_{h} represents the mass of the hydrate, in grams; m_{wf} represents the mass of residual pore water, in grams; M_{h} represents the molar mass of methane hydrate, in g/mol; m_{m} represents the mass of methane required for the hydrate reaction, in grams; R_{mw} represents the residual water content; R_{ms} represents the mass-to-mass ratio of the sediment.

To facilitate comparison with results from other studies, the mass abundance can be converted to saturation using Eq. (2).

$$\begin{cases} S_{\mathrm{h}} = \dfrac{V_{\mathrm{h}}}{V_{\phi}} \times 100\% = \dfrac{m_{\mathrm{h}}}{\rho_{\mathrm{h}} V_{\phi}} \times 100\% = \dfrac{m_{\mathrm{total}}}{\rho_{\mathrm{h}} V_{\phi}} R_{\mathrm{mh}} \\ m_{\mathrm{total}} = m_{\mathrm{h}} + m_{\mathrm{sand}} + m_{\mathrm{soil}} + m_{\mathrm{wf}} \\ V_{\phi} = V_{\mathrm{samp}} - V_{\mathrm{sand}} - V_{\mathrm{soil}} = \dfrac{\pi}{4} d_{\mathrm{samp}}^2 h_{\mathrm{samp}} - \dfrac{m_{\mathrm{sand}}}{\rho_{\mathrm{sand}}} - \dfrac{m_{\mathrm{soil}}}{\rho_{\mathrm{soil}}} \end{cases} \tag{2}$$

In the equation, m_{total} represents the total mass, in grams.

The experimental phenomena and results of sandy hydrate sediments were referred to in reference [22]. This literature reveals the mechanical response characteristics and stress-strain curves of sandy hydrate sediments at saturation levels of 5%, 15%, 25% and 35% through systematic experiments.

Since the synthesis process of argillaceous silt hydrate will displace and replace the original sediment particles and destroy the pore structure of the original sediment, it is more accurate to use the average mass abundance to characterize the content of hydrate [23]. The mass abundance of argillaceous silt hydrate sediments was taken as the preset values of 20%, 40%, 60% and 80%. Triaxial compression experiments were conducted on sandy hydrate sediments under different temperature and pressure conditions. The stress-strain curves obtained are shown in Fig. 6. The analysis of the result graph yields:

(1) With the increase of mass abundance, the peak strength of argillaceous silty hydrate sediments increases significantly. The reason is that as the content of hydrates increases, the supporting effect of hydrates on sediments is enhanced.

(2) With the decrease of temperature, the peak intensity of sandy hydrate sediments increases. The reason is that as the temperature decreases, the cementation between hydrate particles in the sediment intensifies. Meanwhile, the free water that has not formed hydrates will turn into ice with greater strength, which also plays a certain supporting role for the sediment.

(3) The increase in pore pressure will also enhance the peak strength of hydrate sediments to a certain extent.

(4) The stress-strain curve of argillaceous silty hydrate sediments shows a relatively rapid increase in stress within a small strain range, with peak strength present. This is similar to the stress-strain curve of sandy hydrate sediments with higher saturation, but the peak strength is rather

ambiguous and has a smaller value. The reason is that the cementation effect of hydrates and kaolin on sediments is far less than that of epoxy resin.

(5) With the increase of the mass abundance of the hydrated sediment of argillaceous silt, its strain softening characteristics become more obvious. The reason is that the occurrence form of hydrates gradually transitions from pore-filling type, skeleton support type to particle cementation type.

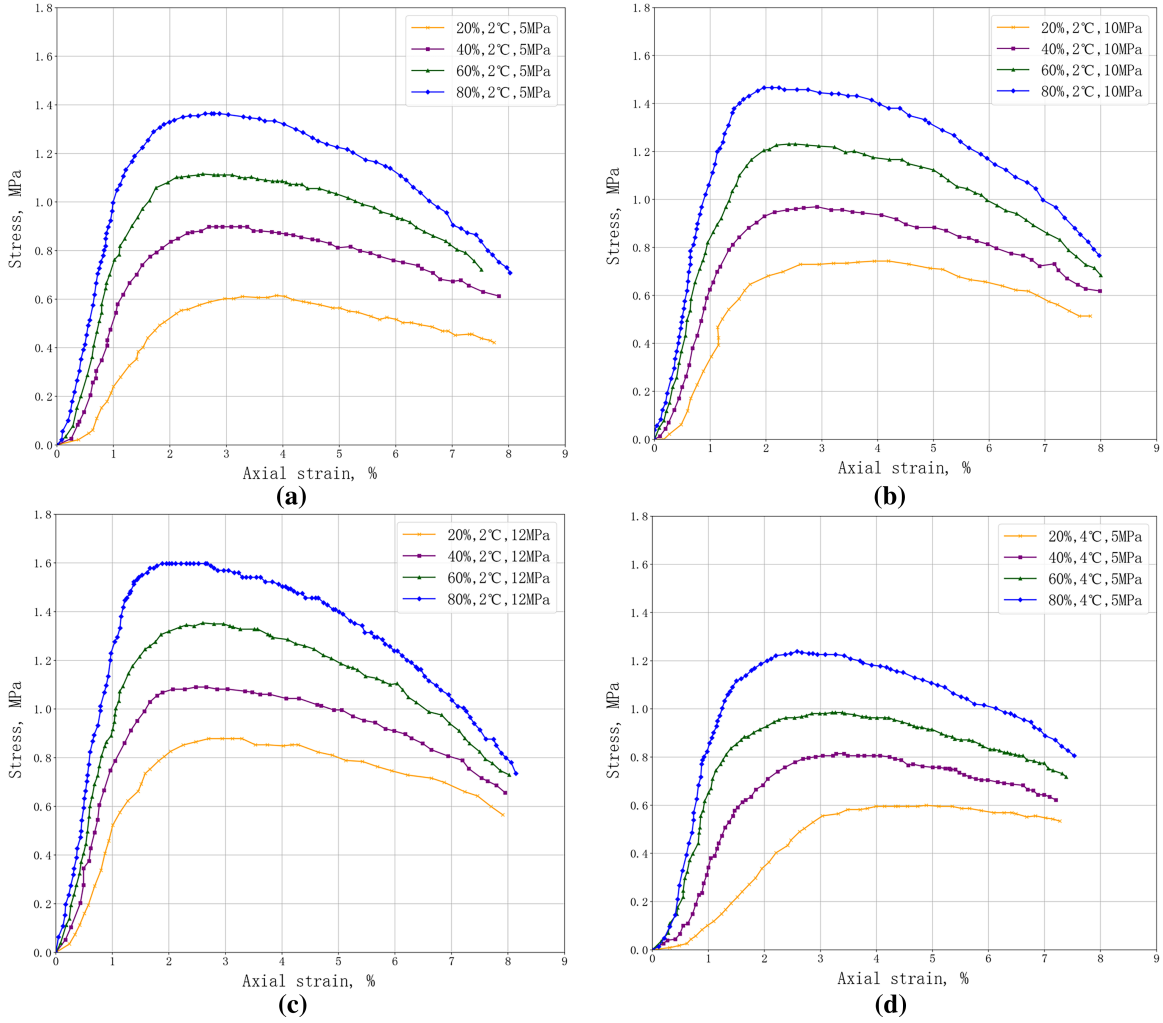

Figure 6: (Continued)

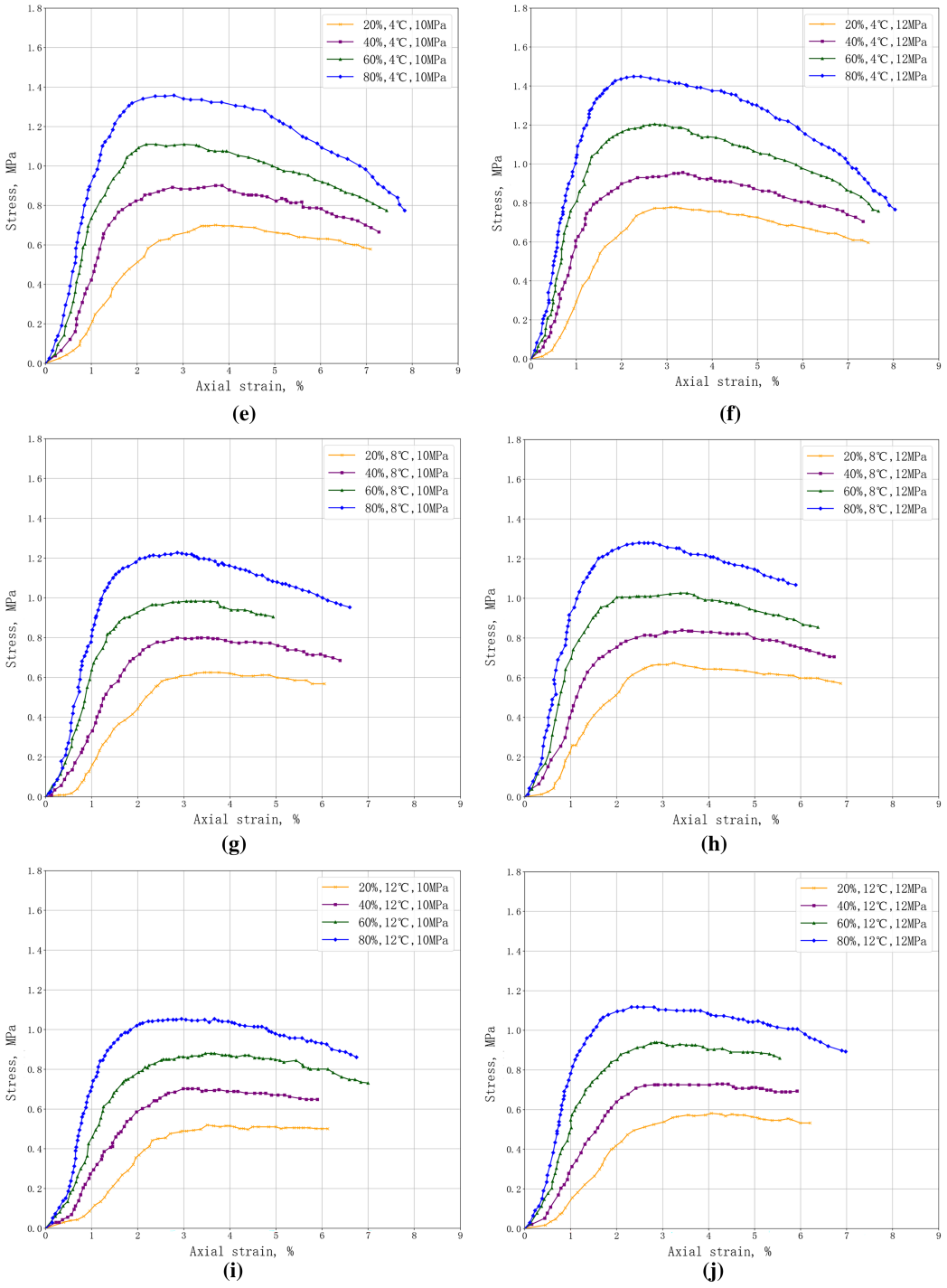

Figure 6: Stress-strain curves of argillaceous silt hydrate deposits under different temperature and pressure conditions: (**a**) The stress-strain curve at 2°C and 5 MPa; (**b**) The stress-strain curve at 2°C and 10 MPa; (**c**) The stress-strain curve at 2°C and 12 MPa; (**d**) The stress-strain curve at 4°C and 5 MPa; (**e**) The stress-strain curve at 4°C and 5 MPa; (**f**) The stress-strain curve at 2°C and 12 MPa; (**g**) The stress-strain curve at 8°C and 10 MPa; (**h**) The stress-strain curve at 8°C and 12 MPa; (**i**) The stress-strain curve at 12°C and 10 MPa; (**j**) The stress-strain curve at 22°C and 12 MPa

The Poisson's ratio calculated based on the results of the uniaxial compression test is shown in Table 1.

Table 1: Poisson's ratio of argillaceous silt hydrate sediments

Quality abundance	Temperature	Pressure	Poisson's ratio	Pressure	Poisson's ratio	Pressure	Poisson's ratio	Average poisson's ratio
20%	2°C	5 MPa	0.33	10 Mpa	0.28	12 MPa	0.26	0.32
	4°C	5 MPa	0.35	10 MPa	0.30	12 MPa	0.29	
	8°C	5 MPa		10 MPa	0.34	12 MPa	0.34	
	12°C	5 MPa		10 MPa	0.35	12 MPa	0.34	
40%	2°C	5 MPa	0.28	10 Mpa	0.26	12 MPa	0.25	0.27
	4°C	5 MPa	0.28	10 MPa	0.26	12 MPa	0.24	
	8°C	5 MPa		10 MPa	0.29	12 MPa	0.28	
	12°C	5 MPa		10 MPa	0.31	12 MPa	0.27	
60%	2°C	5 Mpa	0.23	10 Mpa	0.21	12 MPa	0.21	0.23
	4°C	5 MPa	0.24	10 MPa	0.24	12 MPa	0.22	
	8°C	5 MPa		10 MPa	0.25	12 MPa	0.23	
	12°C	5 MPa		10 MPa	0.26	12 MPa	0.23	
80%	2°C	5 Mpa	0.20	10 Mpa	0.17	12 MPa	0.16	0.19
	4°C	5 MPa	0.19	10 MPa	0.18	12 MPa	0.16	
	8°C	5 MPa		10 MPa	0.19	12 MPa	0.17	
	12°C	5 MPa		10 MPa	0.21	12 MPa	0.21	

Based on the stress-strain curve of the hydrated sediment of argillaceous silt (Fig. 6), the Young's modulus, shear modulus and volumetric modulus of the hydrated argillaceous silt can be calculated. By comparing the results of the hydrated sediment of argillaceous silt under different temperature and pressure conditions, the following conclusions are drawn:

(1) The Young's modulus, shear modulus and volumetric modulus of argillaceous silt hydrate sediments increase significantly with the increase of hydrate saturation. This result indicates that an increase in hydrate content will enhance the strength of hydrate sediments.

(2) The increase in pore pressure and the decrease in temperature will also lead to an increase in strength indicators such as Young's modulus. This is consistent with the law of obtaining the peak strength from the stress-strain curve.

(3) The variation laws of strength indicators such as Young's modulus, shear modulus and volume modulus of argillaceous silt hydrate sediments with saturation (mass abundance), temperature and pore pressure are consistent with those of sandy hydrate sediments, but the values are significantly decreased. The reason might be that the cementation strength of kaolin and hydrates is limited, while the epoxy resin in sandy hydrate sediments provides a greater cementation strength.

By comparing the triaxial compression experimental results of argillaceous silty hydrate sediments and sandy hydrate sediments, the following conclusions are drawn: The average Poisson's ratio of argillaceous silty hydrate is higher than that of sandy hydrate, mainly because the presence of kaolin destroys the pore structure and reduces the compressibility of argillaceous silty. The sandy hydrates, however, exhibit a lower Poisson's ratio due to the rigid cementing effect of epoxy resin. In terms of strength parameters, the Young's modulus, shear modulus and volume modulus of argillaceous silt are all lower than those of sandy hydrates. The high strength of the latter mainly comes from the strong cementing effect of epoxy resin, while the weak cementing property of kaolin in argillaceous silt limits the supporting effect of hydrates. Although with the increase of mass abundance, the hydrate occurrence form of argillaceous silty sand hydrates gradually transitions from pore-filling type to granular cementitious type, its strength is still lower than that of sandy hydrates. From the perspective of the stress-strain curve, although the hydrated argillaceous silt shows peak strength at high quality abundance, its strength is rather ambiguous and the softening characteristics are relatively weak, presenting a low-level strain softening overall. The sandy hydrates show clear peak strength and significant strain softening at a higher saturation level. At a lower saturation level, due to insufficient support, they exhibit strain hardening, with the critical saturation ranging from 15% to 25%. This indicates that the mechanical response of sandy hydrates is controlled by the cementation morphology dominated by hydrate saturation, while the mechanical properties of argillaceous silty hydrates are limited by the weak cementation property of kaolin. The strength enhancement and softening effects of hydrates have always been at a relatively low level. Therefore, the differences in material composition and cementitious mechanism determine that the mechanical properties of argillaceous silty sand hydrates are comprehensively weaker than those of sandy hydrates.

3 Correction Method of Pipe Soil p-y Curve in Shallow Seabed Silty Sand Hydrate Strata

Due to the special mechanical properties of hydrate sediments, the p-y curve of the hydrated strata with argillaceous silt in the shallow seabed is quite different from that of the traditional shallow seabed strata. Based on the API specification, the calculation method of the p-y curve for the shallow seabed hydrate-bearing strata is revised, which is of great significance for improving the safety of Marine drilling and completion operations.

3.1 The Characteristics and Engineering Property Parameters of the Shallow Seabed Strata

Since the supporting force of the deep-water underwater wellhead-shallow string system mainly comes from the shallow seabed strata, the property parameters of the shallow seabed strata are important factors affecting the stability of the deep-water underwater wellhead-shallow string system. The main engineering property parameters of the strata (soil layers) used in this paper when studying the interaction between the shallow seabed strata and the pipe string are as follows:

(1) The underwater specific gravity of soil

Due to the fact that the soil in the shallow strata of the seabed is submerged in water and is subject to the buoyancy of water, the specific gravity will be reduced. Therefore, when calculating, the specific gravity under water (also known as the effective specific gravity) is taken for calculation:

$$\gamma_s' = (\rho_s - \rho_w)\, g \tag{3}$$

where γ_s' is the underwater specific gravity of the soil, N/m^3; ρ_s and ρ_w are the densities of seawater and soil, respectively, and can be taken as 1600∼2200 kg/m^3 and 1025 kg/m^3; g is the gravitational acceleration, 9.81 m/s^2.

(2) Effective oversoil pressure

The effective overlying soil pressure is the overlying soil pressure calculated based on the effective specific gravity of the soil used. In this paper, both the overlying soil pressure and the seawater pressure are jointly defined as the effective overlying soil pressure during the calculation:

$$\sigma_{\mathrm{v}}^{\prime}=\sum_{i=0}^{h}\gamma_{i}^{\prime}h_{i}+\rho_{\mathrm{w}}gh_{\mathrm{w}} \tag{4}$$

where $\sigma_{\mathrm{v}}^{\prime}$ is the effective oversoil pressure, Pa; $\gamma_{i}^{\prime}$ is the underwater specific gravity of the i-th layer of soil, N/m^3; h_i is the thickness of the first layer of soil, m; ρ_{w} is the density of seawater, kg/m^3; g is the gravitational acceleration, 9.81 m/s^2; h_{w} is the depth of the seawater, m.

(3) Shear strength

The shear strength of soil can be calculated according to the Mohr-Coulomb criterion:

$$\tau_{\mathrm{f}}=C+\sigma_{\mathrm{s}}\tan\theta \tag{5}$$

where τ_{f} is the shear strength, Pa; C is the cohesion, Pa; σ_{s} is the normal stress, Pa; θ is the internal friction Angle, °.

(4) Relative density

The relative compactness of cohesive soil can be calculated by Eq. (7) :

$$\rho_{\mathrm{sr}}=\frac{e_{\max}-e_{\mathrm{i}}}{e_{\max}-e_{\min}} \tag{6}$$

where $e_{\max}$ and $e_{\min}$ are respectively the maximum porosity ratio and the minimum porosity ratio in the most loose state; e_{i} is the natural state pore ratio.

(5) Damping coefficient

The damping coefficient can be calculated by Eq. (8) [24] :

$$c\left(z\right)=6\left(\frac{\omega D_{\mathrm{c}}}{V_{\mathrm{s}}}\right)^{-\frac{1}{4}}\rho_{\mathrm{s}}V_{\mathrm{s}}D_{\mathrm{c}}+2\beta_{\mathrm{s}}\frac{1.2E_{\mathrm{s}}}{\omega} \tag{7}$$

where ω is the vibration frequency, Hz; D_{c} is the diameter of the pipe pile, m; V_{s} is the shear wave velocity of soil, m/s; ρ_{s} is the density of soil, g/m^3; β_{s} is the damping ratio, it is generally taken as 0.05; E_{s} is the Young's modulus of soil.

3.2 Calculation of Engineering Property Parameters of Argillaceous Silt Hydrate Sediments

Since the hydrated sediment of argillaceous silt is closer to the actual situation of the shallow seabed strata, triaxial compression experiments were conducted on the hydrated sediment of argillaceous silt under different confining pressures, and its engineering property parameters were calculated based on the experimental results.

(1) Experimental Procedures

The materials and steps for preparing silty silt hydrate sediments are detailed in Sections 2.1 and 2.2 on the materials and equipment for preparing natural gas hydrate sediments. The experimental steps of triaxial compression are basically the same as those in Section 2.4. However, it should be noted that during the experiment, while ensuring the constant pore pressure, the effective confining pressure should be controlled at the set value through the confining pressure control system.

(2) Experimental Results and Analysis

Triaxial compression experiments were conducted respectively under the effective confining pressure conditions of 1.0, 2.0 and 3.0 MPa. During the experiments, the pore pressure was maintained at 4 MPa. The experimental results are shown in Fig. 7.

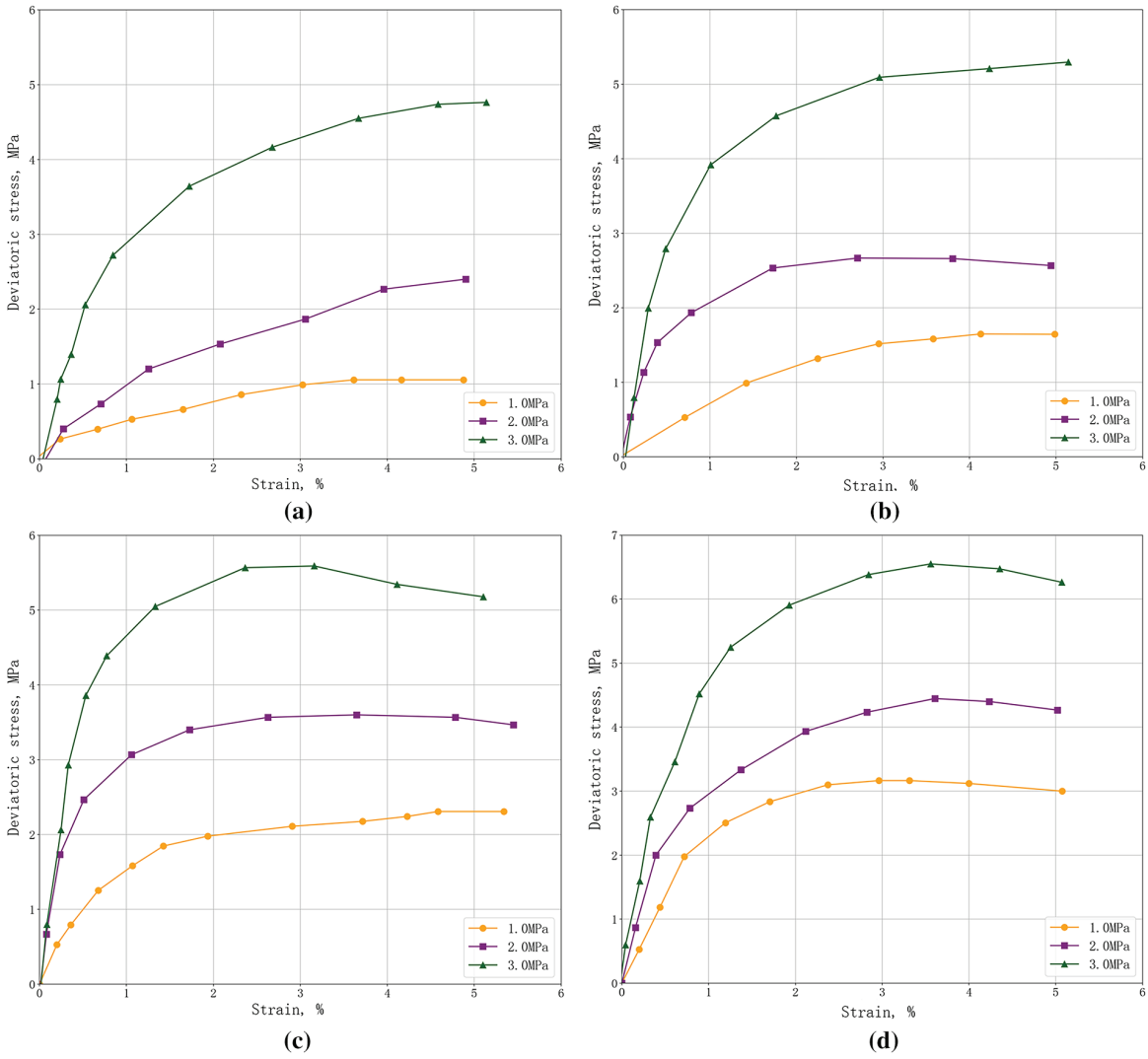

Figure 7: Triaxial shear test stress-strain curves with different saturation: (**a**) Stress-strain curve at 0% saturation; (**b**) Stress-strain curve at 10% saturation; (**c**) Stress-strain curve at 20% saturation; (**d**) Stress-strain curve at 30% saturation

By analyzing the stress-strain curves of argillaceous silt hydrate sediments under different net confining pressures (Fig. 7), it can be found that the peak strength of argillaceous silt hydrate sediments increases with the increase of effective confining pressure.

Based on the stress-strain curves obtained from the triaxial compression experiment, the Mohr circle was plotted by MATLAB programming (Fig. 8) to calculate the internal friction Angle and cohesion. The calculation formula is as follows (Eq. (8)).

$$\begin{cases} E = \left| \dfrac{\sigma_{\mathrm{d}}}{\varepsilon_{\mathrm{a}}} \right| \\ \nu = \left| \dfrac{\varepsilon_{\mathrm{r}}}{\varepsilon_{\mathrm{a}}} \right| \\ G = \dfrac{E}{2\,(1+\nu)} \\ K = \dfrac{E}{3\,(1-2\nu)} \end{cases} \tag{8}$$

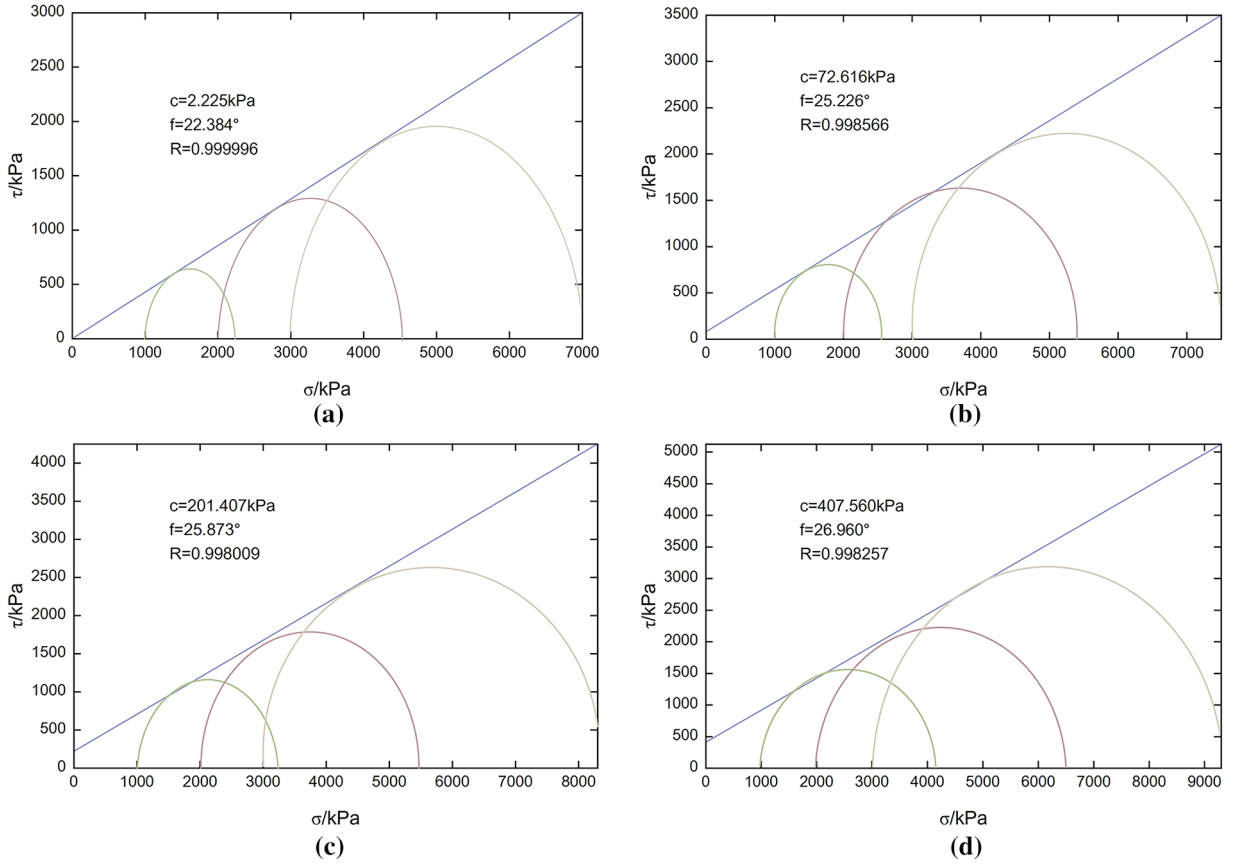

Figure 8: Stress-strain curve of triaxial shear test for samples with different saturation (**a**) The Mohr circle at 0% saturation; (**b**) The Mohr circle at 10% saturation; (**c**) The Mohr circle at 20% saturation; (**d**) The Mohr circle at 30% saturation

The calculation results are shown in Table 2.

Table 2: Cohesion, internal friction angle and Young's modulus of argillaceous silt hydrate deposits

Saturation (%)	Cohesion (kPa)	Internal friction angle (°)	Young's modulus (MPa)
0	2.23	23.38	40.32
10	72.62	25.23	61.55
20	201.41	25.87	102.62
30	407.56	26.96	163.61

By analyzing the cohesion, internal friction Angle and Young's modulus of the hydrated argillous silt (Table 1), the following conclusions are mainly drawn:

(1) The cohesion of argillaceous silt hydrate sediments increases significantly with the increase of saturation.

(2) Under the experimental conditions of this paper, the internal friction Angle of the hydrated argillaceous silt sediment increases with the increase of saturation.

(3) By comparing with the data in Table 1, it can be found that the existence of confining pressure will significantly increase the Young's modulus of the hydrated sediment of argillaceous silt.

3.3 Correction of the p-y Curve in Hydrate Sediment Strata

Although advanced finite element software like ABAQUS can meticulously simulate the pipe-soil interaction in hydrate-bearing strata, the modeling process is complex and computationally expensive, making it difficult to be widely adopted for preliminary engineering design, parametric sensitivity analysis, or rapid safety assessment. Therefore, developing an accurate yet simplified analytical p-y curve correction formula is of significant practical engineering value. The objective of this study is not to replace finite element analysis but to derive a simplified design formula, analogous to the API specification, for clayey-silt hydrate formations based on high-fidelity FEM results. This formula aims to assist engineers in scenarios where performing sophisticated numerical simulations is not feasible.

(1) The calculation method of p-y curve in API specification

The p-y curve of the API standard was proposed by Matlock [25] and Reese et al. [26] based on experiments and is used for calculating the lateral foundation reaction force on the pipe side per unit area of sandy soil in shallow seabed strata:

$$p\left(y\right)=\kappa p_{\mathrm{u}}\tanh\left(\frac{K_{\kappa}z}{\kappa p_{\mathrm{u}}}y\right) \tag{9}$$

where κ is the periodic or continuous static load coefficient, which can be calculated by Eq. (11); p_{u} is the lateral ultimate foundation reaction force of the foundation, kPa, it can be calculated by Eq. (11); kN/m; K_{κ} is the initial modulus coefficient of the reaction force of the sandy soil foundation, N/m^3; z is the depth, m.

$$\begin{cases}\kappa=\left(3.0-0.8h/D_{\mathrm{c}}\right), & \text{for static loads}\\ \kappa=0.9, & \text{for periodic loads}\end{cases} \tag{10}$$

where h is the height, m; D_c is the diameter of the pipe pile, m.

$$\begin{cases} p_{us} = (C_1 z + C_2 D_c)\,\gamma_s' z, \text{ when } z < z_r; \\ p_{ud} = C_3 D_c \gamma_s' z, \text{ when } z \geq z_r; \\ z_r = \dfrac{C_3 - C_2}{C_1} D_c \end{cases} \tag{11}$$

where γ_s' is the underwater specific gravity of the soil, N/m^3; z_r is the boundary depth between deep and shallow soil, m; C_1, C_2, C_3 related to the internal friction Angle.

In the API specification method, C_1, C_2, C_3 are calculated by Eq. (12):

$$\begin{cases} C_1 = \dfrac{k_0 \tan\theta \sin\beta}{\tan(\beta-\theta)\cos\alpha} + \dfrac{\tan^2\beta \tan\alpha}{\tan(\beta-\theta)} + k_0 \tan\beta\,(\tan\theta \sin\beta - \tan\alpha) \\ C_2 = \dfrac{\tan\beta}{\tan(\beta-\theta)} - k_\alpha \\ C_3 = k_\alpha\left(\tan^8\beta - 1\right) + k_0 \tan\theta \tan^4\beta \end{cases} \tag{12}$$

where θ is the internal friction Angle, °; $k_0 = 0.4$, $\alpha = \theta/2$, $\beta = 45^\circ + \theta/2$,$k_\alpha = \tan^2(45^\circ - \theta/2)$.

Li [28] obtained the calculation methods of the formulas for calculating the internal friction angles of C_1, C_2, C_3 and K_κ (ϕ) based on the regression of Figs. 9 and 10:

$$\begin{cases} C_1(\theta) = 1.66715 \times 10^{-4}\theta^3 - 7.29 \times 10^{-3}\theta^2 + 0.16345\theta - 0.93304 \\ C_2(\theta) = -3.3333 \times 10^{-5}\theta^3 + 5.57143 \times 10^{-3}\theta^2 - 0.10345\theta + 1.66071 \\ C_3(\theta) = 4 \times 10^{-4}\theta^4 - 0.033333\theta^3 + 1.11\theta^2 - 16.1667\theta + 90 \end{cases} \tag{13}$$

where θ is the internal friction Angle of the sandy soil, °.

$$\begin{cases} K_\kappa(\varphi) = 4.676 \times 10^{-4}\theta^3 + 0.114655\theta^2 - 6.60665\theta + 92.38, b\text{elow the groundwater level} \\ K_\kappa(\varphi) = -4.632 \times 10^{-3}\theta^3 + 0.7431\theta^2 - 28.713\theta + 330.26, \text{above the groundwater level} \end{cases} \tag{14}$$

where $K_\kappa(\theta)$ is the initial modulus coefficient of the reaction force of the sandy soil foundation, $\times 10^6$ N/m^3.

(2) Calculation of the p-y curve of the hydrated strata with argillaceous silt in the shallow seabed

The ABAQUS finite element simulation software was used to numerically simulate the hydrate-bearing strata with different saturations, and the p-y curves of the hydrated strata with muddy silty sand in the shallow seabed were calculated. The relevant parameters of the hydrated strata with muddy silty sand used were obtained from the previous experiments, and the basic parameters of the pipe piles are shown in Table 3.

When modeling, the loads on the riser pipe and the wellhead are simplified to one wellhead load. The pipe pile is regarded as the ideal linear elastic material, and the formation is regarded as the ideal elastoplastic material. The Mohr-Coulomb constitutive model is adopted. Both the pipe and the soil adopt 8-node 3D solid units. The contact between the pipe pile and the soil is in a surface-to-surface contact state. The contact attribute is selected as friction, and the constraint condition is selected as the penalty function. The modeling situation is shown in Fig. 11.

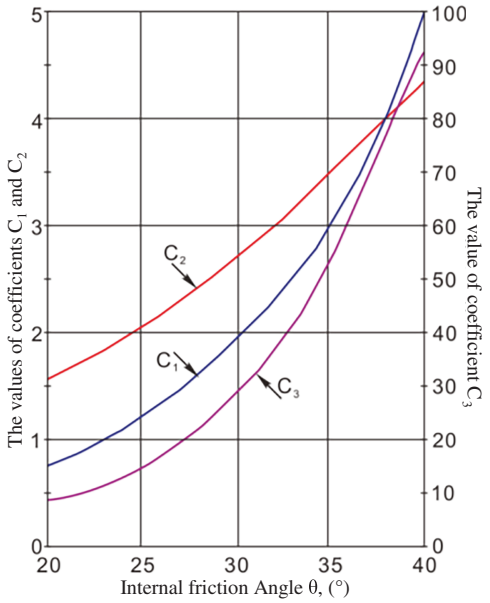

Figure 9: Relationship between C_1, C_2, C_3 and internal friction angle [27]

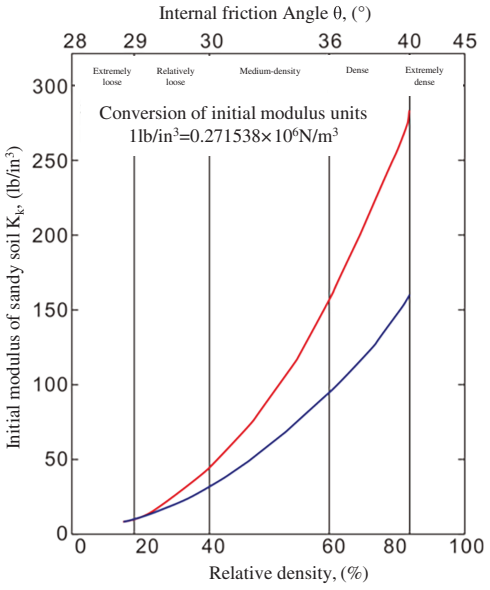

Figure 10: Relationship between K_κ and internal friction angle [27]

Table 3: Basic parameters of pipe piles

Outer diameter	Wall thickness	Elastic modulus	Poisson ratio	Density
0.914 m	0.0254 m	210 GPa	0.33	7580 kg/m^3

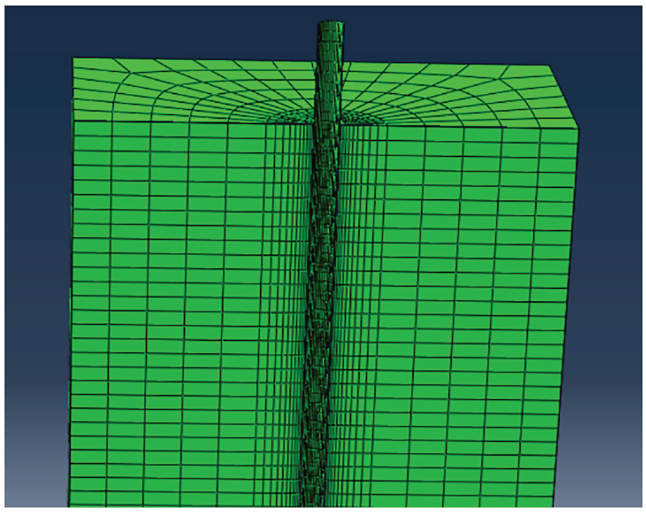

Figure 11: Establishment and meshing of pipe model and subsea shallow strata model

To accurately simulate the pipe-soil interaction, a three-dimensional finite element model was established. The soil domain was modeled as a cylinder with a diameter of 10 m and a depth of 15 m, dimensions sufficiently large to minimize boundary effects on the pipe response. The boundary conditions were defined as follows: the bottom surface was fixed in all directions (U1 = U2 = U3 = 0), the lateral surface was constrained in the radial direction but free in the vertical direction, and the top surface was set as a free surface. Surface-to-surface contact was defined between the pipe and the soil, with a friction coefficient of 0.4. The constraint enforcement method was set to the penalty algorithm. Both the pipe and the soil were discretized using C3D8R elements (8-node linear brick, reduced integration), with a refined mesh in the contact zone to ensure computational accuracy.

According to the results of the finite element simulation, the calculated p-y curve is shown in Fig. 12.

According to the p-y curve calculated by ABAQUS (Fig. 12), it can be found that under the same displacement conditions, with the increase of hydrate saturation, the foundation reaction force of the formation increases significantly. The reason is that the increase in hydrate saturation will enhance the strength of the sediment, which is consistent with the law obtained in the previous text.

Based on a series of p-y curves calculated from the ABAQUS finite element model (Fig. 12), a Python optimization algorithm was developed. Its purpose was to inversely fit a unified, parameterized mathematical expression for the p-y curves that is applicable across all saturation levels. This expression, introduced with a cementation factor related to mass abundance and a displacement correction term (as shown in Eq. (15)), generalizes the discrete FEM data points into a continuous functional model with clear physical significance, thereby greatly enhancing its engineering applicability. The p-y curve is shown in Fig. 13.

$$\alpha = 0.37\theta$$
$$K_{\kappa} = 850\ \mathrm{kN/m^3} \tag{15}$$

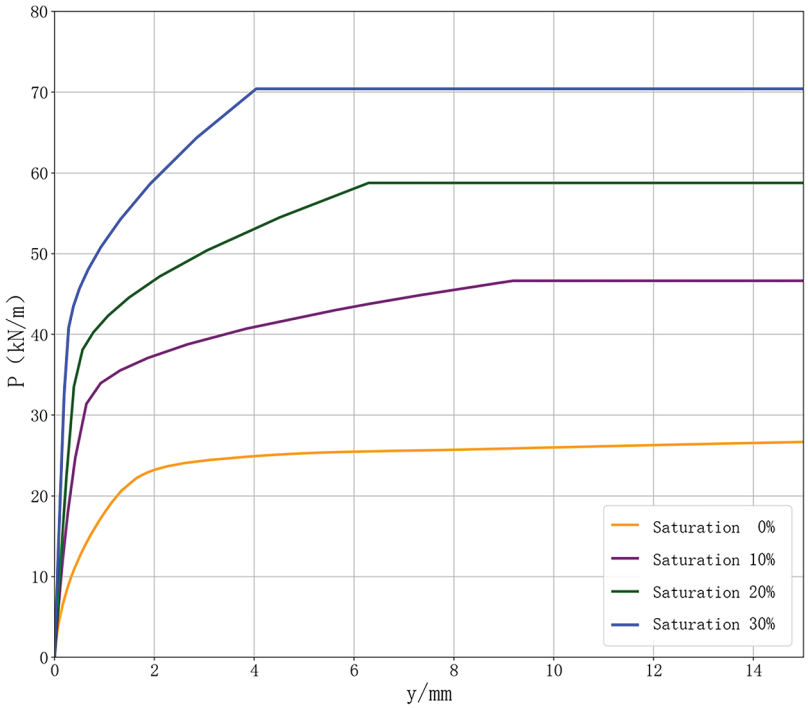

Figure 12: p-y curves calculated by ABAQUS

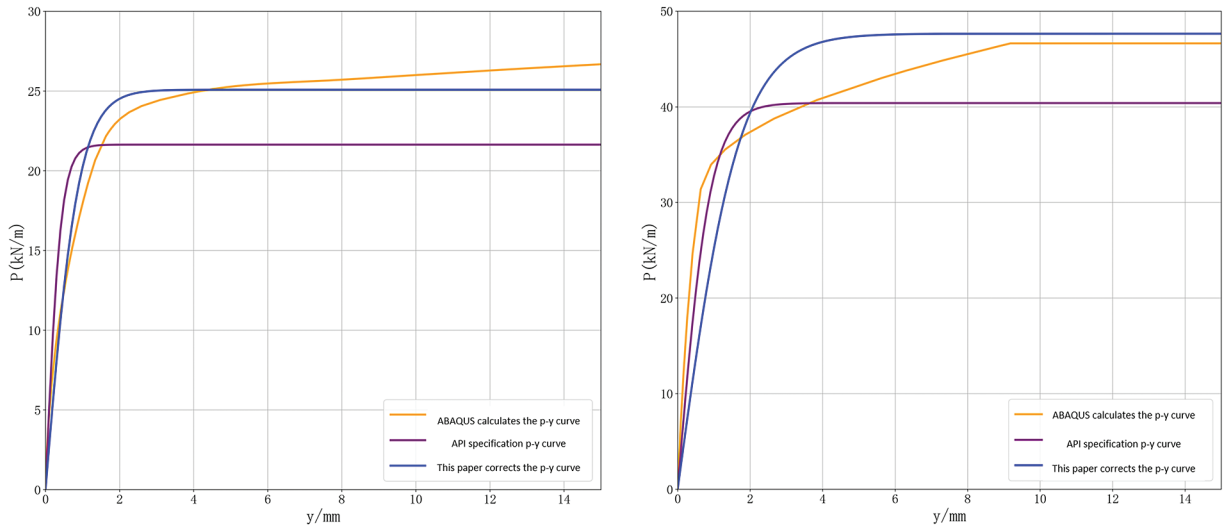

Figure 13: (Continued)

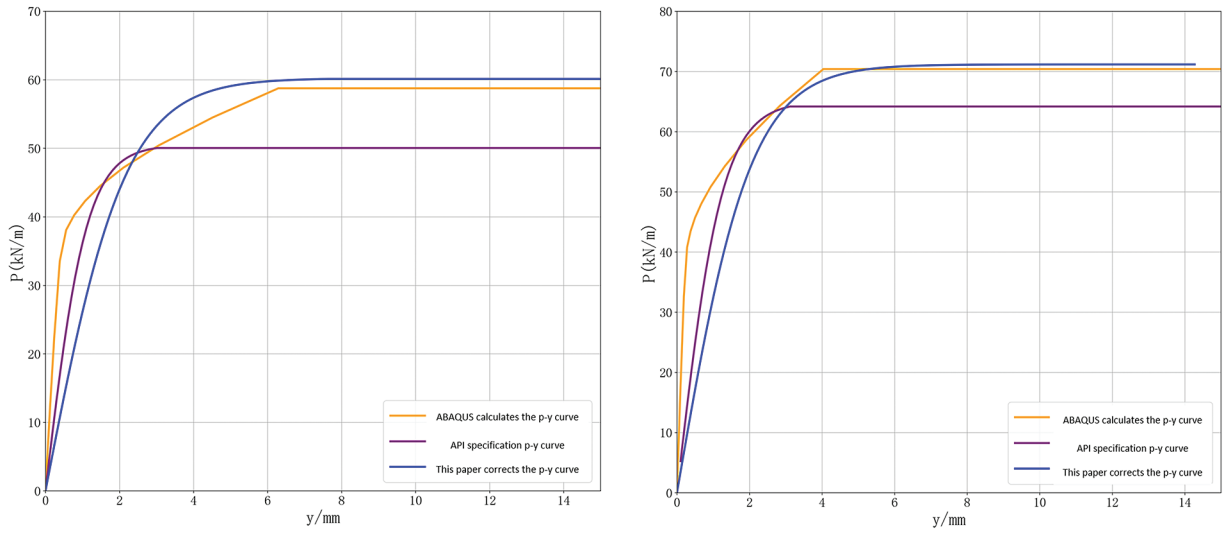

Figure 13: p-y curves of formations with different hydrate saturations: (**a**) 0% hydrate saturation p-y curve; (**b**) 10% hydrate saturation p-y curve; (**c**) 20% hydrate saturation p-y curve; (**d**) 30% hydrate saturation p-y curve

In order to analyze the advantages and disadvantages of the corrected method in this paper, the error rate calculation Formula (16) was defined, and the calculation results are shown in Fig. 14.

$$\begin{cases} \xi_{\mathrm{A}} = \dfrac{p_{\mathrm{ABA}} - p_{\mathrm{API}}}{p_{\mathrm{ABA}}} \\ \xi_{\mathrm{c}} = \dfrac{p_{\mathrm{ABA}} - p_{\mathrm{cal}}}{p_{\mathrm{cal}}} \end{cases} \tag{16}$$

where ξ_{A} and ξ_{c} represent the error rates of the calculation method of the API specification and the calculation method corrected in this paper; p_{ABA} is the foundation reaction force calculated for ABAQUS, kN/m; p_{API} is the foundation reaction force calculated for the calculation method of the API specification, kN/m; p_{cal} is the foundation reaction force calculated by the modified calculation method for this paper, kN/m.

$$\xi_{\mathrm{c}} = \sum_{j=1}^{4} \left(\frac{\sum_{i=1}^{n} |\xi_{\mathrm{API}}| - \sum_{i=1}^{n} |\xi_{\mathrm{cal}}|}{n} \right) \tag{17}$$

where ξ_{c} is the relative error rate.

According to Eq. (17), the relative error rates of the modified p-y curve calculation method of the shallow seabed strata in this paper and the p-y curve calculation method of the API specification were calculated $\xi_{\mathrm{c}} = 17.92\%$.

Based on the error comparison (see Fig. 14) and the analysis of the relative error rate between the p-y curve calculation method modified in this paper and the p-y curve calculation method of the API specification, it can be found that the p-y correction method for the shallow seabed hydrate-bearing strata proposed in this paper is significantly superior to the p-y curve calculation method of the API specification.

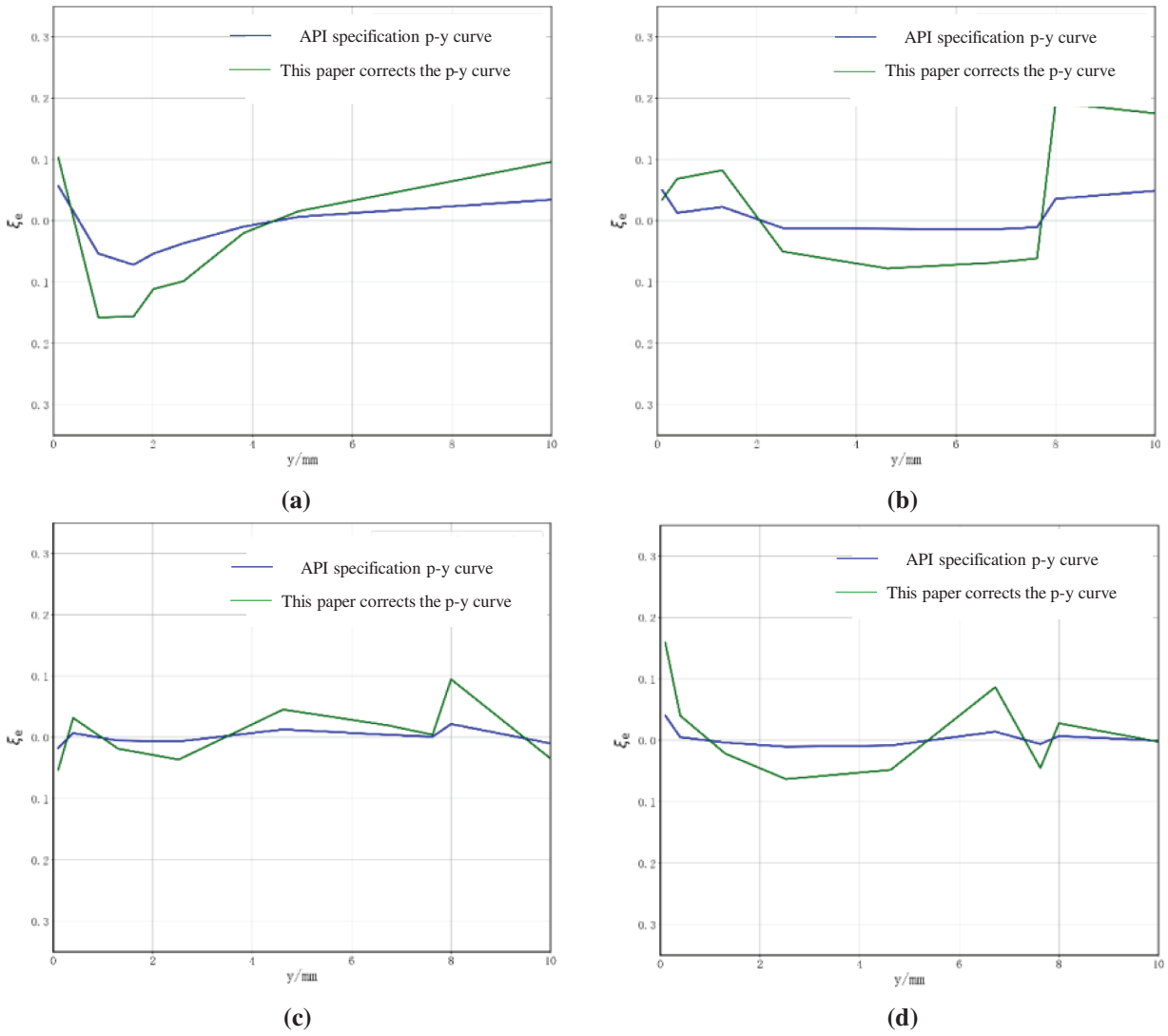

Figure 14: Error comparison of p-y curves: (**a**) Comparison of p-y curve errors with 0% hydrate saturation; (**b**) Comparison of p-y curve errors with 10% hydrate saturation; (**c**) Comparison of p-y curve errors with 20% hydrate saturation; (**d**) Comparison of p-y curve errors with 30% hydrate saturation

4 Conclusions and Suggestions

Triaxial compression experiments were conducted on sandy and argillaceous silt hydrate sediments using a self-developed triaxial-seepage experimental platform for hydrates. The triaxial compression experimental failure phenomenon of sandy hydrate sediments is similar to that of traditional cores, but the failure phenomenon of argillaceous silty hydrate sediments is manifested as compression dispersion. The reason is that hydrates and kaolin cannot play a good role in consolidating sediments.

The stress-strain curve of argillaceous silty hydrate sediments shows the strain softening characteristics of rapid stress increase and weakening within a small strain range. Although its peak strength is similar to that of highly saturated (25%–35%) sandy hydrates, the strength is ambiguous and the value

is significantly low. With the increase of mass abundance to 80%, the strain softening characteristics of argillaceous silt are enhanced, which is related to the transition of the hydrate occurrence form from pore-filling type to granular cementing type. In contrast, sandy hydrates show clear peak strength and significant strain softening at high saturation due to the strong cementation of particles. When the saturation is low (5%–15%), due to insufficient hydrate support, the curve has no peak value and shows strain hardening, and the critical saturation is between 15% and 25%. The mechanical property differences of argillaceous fine sand stem from the weak cementation of kaolin and the limitation of the occurrence form of hydrates: Even if the abundance increases and promotes the transformation of the cementation form, its strength is still much lower than the rigid cementation of epoxy resin in sandy hydrates, resulting in blurred peaks, low modulus, and the overall strength is always weaker than that of the sandy system.

With the increase of saturation and average mass abundance, the strength indicators such as the peak strength of the stress-strain curve and Young's modulus of the hydrated sediments of sandy and argillaceous silty sand have significantly increased. The reason is that the supporting effect of hydrates on sediments increases with the increase of hydrate content. Meanwhile, the increase in pore pressure will also lead to an increase in the strength of hydrate sediments.

With the decrease of temperature, the strength indicators such as the peak strength of the stress-strain curve and Young's modulus of the hydrated sediments of sandy and argillaceous silty sand all increase. The reason is that as the temperature decreases, the cementation between hydrate particles in the sediment intensifies. Meanwhile, the free water that has not formed hydrates will turn into ice with greater strength, which also plays a certain supporting role for the sediment.

Under the experimental conditions of this paper, the cohesion, internal friction Angle and Young's modulus of the hydrated argillaceous silt sediment increase with the increase of saturation (mass abundance). The increase of confining pressure will cause a significant increase in Young's modulus.

The presence of hydrates will enhance the strength of sediments. Under the same displacement conditions, the foundation reaction force of hydrate-containing strata is significantly greater than that of conventional strata. The relative error rate between the p-y curve calculation method of API specification and the p-y curve calculation method of hydrate-bearing strata proposed in this paper is 17.92%. Therefore, the p-y curve correction calculation method for hydrate-bearing strata proposed in this paper has obvious superiority and is more in line with the actual situation of shallow hydrate-bearing strata on the seabed.

Acknowledgement: This work was supported by The National Key Research and Development Program of China (2022YFC2806403).

Funding Statement: The National Key Research and Development Program of China (2022YFC280 6403).

Author Contributions: The authors confirm contribution to the paper as follows: study conception and design: Haoyu Diao, Bangchen Wu and Yan Xia; investigation: Fansheng Ban; data collection: Hao Wang and Chaowei Li; analysis and interpretation of results: Li Fu, Henglin Yang and Kailong Wang; draft manuscript preparation: Aiguo He, Xiangyang Wang and Pan Fu; writing—review & editing: Song Deng. All authors reviewed the results and approved the final version of the manuscript.

Availability of Data and Materials: The authors confirm that the data supporting the findings of this study are available within the article.

Ethics Approval: Not applicable.

Conflicts of Interest: The authors declare no conflicts of interest to report regarding the present study.

References

1. Makogon YF, Holditch SA, Makogon TY. Natural gas-hydrates—A potential energy source for the 21st Century. J Pet Sci Eng. 2007;1(3):14–31. doi:10.1016/j.petrol.2005.10.009.
2. Chong ZR, Yang SHB, Babu P, Linga P, Li XS. Review of natural gas hydrates as an energy resource: prospects and challenges. Appl Energy. 2016;162:1633–52. doi:10.1016/j.apenergy.2014.12.061.
3. Wallmann K, Pinero E, Burwicz E, Haeckel M, Hensen C, Dale A, et al. The global inventory of methane hydrate in marine sediments: a theoretical approach. Energies. 2012;5(7):2449–98. doi:10.3390/en5072449.
4. Zhao Y, Kong L, Liu L, Liu J. Influence of hydrate exploitation on stability of submarine slopes. Nat Hazards. 2022;113(1):719–43. doi:10.1007/s11069-022-05321-y.
5. Boswell R, Collett TS, Frye M, Shedd M, McConnell DR, Shelander D. Subsurface gas hydrates in the northern Gulf of Mexico. Mar Petrol Geol. 2012;34(1):4–30. doi:10.1016/j.marpetgeo.2011.10.003.
6. Wang Z, Zhang Y, Peng Z, Shan Z, Sun B, Sun J. Recent advances in methods of gas recovery from hydrate-bearing sediments: a review. Energy Fuels. 2022;36(11):5550–93. doi:10.1021/acs.energyfuels.2c00511.
7. Yu YS, Zhang XW, Liu JW, Lee YH, Li XS. Natural gas hydrate resources and hydrate technologies: a review and analysis of the associated energy and global warming challenges. Energy Environ Sci. 2021;14(11):5611–68.
8. Ning FL, Liang JQ, Wu NY, Zhu YH, Wu SG, Liu CL, et al. Reservoir characteristics of natural gas hydrates in China. Natural Gas Industry. 2020;40(8):1–24. (In Chinese). doi:10.3787/j.issn.1000-0976.2020.08.001.
9. Ye JL, Qin XW, Xie WW, Lu HL, Ma BJ, Qiu HJ, et al. Main progress of the second gas hydrate trial production in the South China Sea. Geology in China. 2020;47(3):557–68. doi:10.12029/gc20200301.
10. Liu C, Meng Q, He X, Li C, Ye Y, Zhang G, et al. Characterization of natural gas hydrate recovered from Pearl River Mouth basin in South China Sea. Mar Pet Geol. 2015;61(4):14–21. doi:10.1016/j.marpetgeo.2014.11.006.
11. Yoneda J, Masui A, Konno Y, Jin Y, Egawa K, Kida M, et al. Mechanical properties of hydrate-bearing turbidite reservoir in the first gas production test site of the Eastern Nankai Trough. Mar Pet Geol. 2015;66(2):471–86. doi:10.1016/j.marpetgeo.2015.02.029.
12. Yoneda J, Oshima M, Kida M, Kato A, Konno Y, Jin Y, et al. Pressure core based onshore laboratory analysis on mechanical properties of hydrate-bearing sediments recovered during India's National Gas Hydrate Program Expedition (NGHP) 02. Mar Pet Geol. 2019;108(1):482–501. doi:10.1016/j.marpetgeo.2018.09.005.
13. Delli ML, Grozic JLH. Prediction performance of permeability models in gas-hydrate-bearing sands. SPE J. 2013;18(2):274–84. doi:10.2118/149508-pa.
14. Roosta H, Khosharay S, Varaminian F. Experimental study of methane hydrate formation kinetics with or without additives and modeling based on chemical affinity. Energy Convers Manag. 2013;76(1):499–505. doi:10.1016/j.enconman.2013.05.024.
15. Chen H, Du H, Shi B, Shan W, Hou J. Mechanical properties and strength criterion of clayey sand reservoirs during natural gas hydrate extraction. Energy. 2022;242(1):122526. doi:10.1016/j.energy.2021.122526.
16. Zhao Y, Liu J, Sang S, Hua L, Kong L, Zeng Z, et al. Experimental investigation on the permeability characteristics of methane hydrate-bearing clayey-silty sediments considering various factors. Energy. 2023;269(24):126811. doi:10.1016/j.energy.2023.126811.
17. Lu W, Zhang G. New p-y curve model considering vertical loading for piles of offshore wind turbine in sand. Ocean Eng. 2020;203(4):107228. doi:10.1016/j.oceaneng.2020.107228.

18. Zhu J, Yu J, Huang M, Shi Z, Shen K. Inclusion of small-strain stiffness in monotonic p-y curves for laterally loaded piles in clay. Comput Geotech. 2022;150(4):104902. doi:10.1016/j.compgeo.2022.104902.
19. Chang BJ, Hutchinson TC. Experimental evaluation of p-y curves considering development of liquefaction. J Geotech Geoenviron Eng. 2013;139(4):577–86. doi:10.1061/(asce)gt.1943-5606.0000802.
20. Dash S, Rouholamin M, Lombardi D, Bhattacharya S. A practical method for construction of p-y curves for liquefiable soils. Soil Dyn Earthq Eng. 2017;97(5):478–81. doi:10.1016/j.soildyn.2017.03.002.
21. Lim H, Jeong S. Simplified p-y curves under dynamic loading in dry sand. Soil Dyn Earthq Eng. 2018;113(1):101–11. doi:10.1016/j.soildyn.2018.05.017.
22. Diao HY, Fan HH, Ji RY, Wu BC, Ye YG, Liu YH, et al. PY curve correction of shallow seabed formation containing hydrate. Energies. 2023;16(7):3274. doi:10.3390/en16073274.
23. Yan L, Dong L. Evaluation system of mechanical parameters of hydrate sandy reservoirs is not applicable to hydrate reservoirs in the south china sea. In: 2020 China Earth Sciences Joint Academic Conference; 2020 Oct 18–21; Chongqing, China. (In Chinese). p. 49–51. doi:10.26914/c.cnkihy.2020.058920.
24. Makris N, Gazetas G. Dynamic pile-soil-pile interaction. Part II: lateral and seismic response. Earthq Eng Struct Dyn. 1992;21(2):145–62. doi:10.1002/eqe.4290210204.
25. Matlock H. Correlation for design of laterally loaded piles in soft clay. In: Offshore Technology Conference; 1970 Apr 21–23; Houston, TX, USA. OTC-1204-MS.
26. Reese LC, Cox WR, Koop FD. Analysis of laterally loaded piles in sand. Paper presented at: The Offshore Technology Conference; 1974 May 5–7; Houston, TX, USA. doi:10.4043/2080-MS.
27. Su KH. Analysis on mechanical stability of subsea wellhead and bearing capacity of conductor for deepwater drilling. Qingdao, China: China University of Petroleum (East China); 2009. (In Chinese).
28. Li YR. Research on lateral dynamic response of pile foundation in liquefied soil layer. Harbin, China: Institute of Engineering Mechanics, China Earthquake Administration; 2006. (In Chinese).